Journal of Materials Chemistry C

ROYAL SOCIETY OF CHEMISTRY

PAPER

View Article Online
View Journal | View Issue

Cite this: J. Mater. Chem. C, 2024, 12, 2561

Quaternary $CsPbX_3$ (X = $Cl_{1-x}Br_x$, $Br_{1-x}I_x$) alloy microplates synthesized by single-step chemical vapor deposition and their two-photon absorption (TPA) properties†

Mohammad Kamal Hossain, [ab] Wayesh Qarony, [de] Ying Wang, [a] Cheuk Kai Gary Kwok, [a] Kingsley O. Egbo, [a] Yuen Hong Tsang, [e] Johnny C. Ho [c] and Kin Man Yu *[ac]

Received 1st September 2023,
Accepted 4th January 2024

DOI: 10.1039/d3tc03166g

rsc.li/materials-c

Because of their well-defined light–matter interaction volume, high-quality single-crystalline nature, and precise bandgap tunability, all-inorganic cesium lead halide ($CsPbX_3$ (X = Cl, Br, I)) perovskite (IHP) microplates are of fundamental and technological interest today. Here, we report the synthesis and properties of ternary $CsPbX_3$ (X = Cl, Br, I) and quaternary $CsPbX_3$ (X = $Cl_{1-x}Br_x$, $Br_{1-x}I_x$) alloy microplates grown by the single-step chemical vapor deposition (CVD) process. Smooth-faceted, single crystalline IHP alloy microplates with good vertical and lateral composition uniformity are achieved. These microplates exhibit strong photoluminescence and are thermally stable with no observable photodegradation. More importantly, two-photon absorption (TPA) is demonstrated in quaternary $CsPb(Cl_{1-x}Br_x)_3$ and $CsPb(Br_{1-x}I_x)_3$ IHP alloy microplates, which adds a new dimension to the functionalities of IHP microplates for nonlinear optical (NLO) applications. We believe that this work will open up multiple avenues for the development of microstructure compatible integrated optoelectronic and photonic applications and will certainly enhance the fundamental NLO research.

1 Introduction

Organometallic halide perovskites (OHPs) have been in the research spotlight due to their unique optoelectronic properties, including high charge carrier mobility ($\sim 50\ cm^2\ V^{-1}\ s^{-1}$),[1] long electron–hole diffusion length ($>1\ \mu m$),[2] strong optical absorption,[3] and direct bandgap.[4] Most notably, great progress has been made in OHP solar cells in just over a decade, and a very high-power conversion efficiency (PCE) of $\eta \approx 26.1\%$ has been achieved.[5] However, the advancement of OHP devices is strongly hampered by several factors, such as the poor thermal stability and hygroscopic nature of the organic cation group[6–9] and the formation of photoinduced trap states and ion migration in OHPs.[9,10] Unlike OHPs, all-inorganic cesium lead halide perovskites (IHPs) have shown excellent open air and thermal stabilities.[11–15] Moreover, similar to the OHPs, IHPs exhibit narrow-intense optical emissions (~tens of milli-electron volts),[16] high photoluminescence quantum yields (PLQY ~90%),[17] and low exciton binding energies (~tens of milli-electron volts)[18] and thus have attracted much recent attention as alternatives to OHP materials. Although solar cells fabricated using IHPs have not attained as high an efficiency as OHP cells, a PCE (η) of ~18% has been reported.[19] However, most reported studies on IHPs were based on materials synthesized by solution processes and hence the quality of materials was relatively poor. Furthermore, the ternary IHPs, $CsPbCl_3$, $CsPbBr_3$, and $CsPbI_3$, have distinctive band gap emissions at ~413 nm, ~529 nm, and ~715 nm, respectively. These discrete bandgaps and the lack of continuously tunable bandgap values limit their device applications.[20,21]

It was also reported that the pure ternary $CsPbX_3$ (X = Cl, Br, I) IHPs were vulnerable to crystalline phase stability issues.[20,22,23] At high temperature (*e.g.*, ≥47 °C for $CsPbCl_3$; ≥130 °C for $CsPbBr_3$; and ≥305 °C for $CsPbI_3$), the stable phase of all IHPs is found to be cubic.[20] This cubic phase usually transforms into the room temperature phase. For instance, bulk $CsPbI_3$ has a cubic stable phase also called the black phase at ≥305 °C. As the material is cooled down gradually to room temperature, the black cubic

[a] Department of Physics, City University of Hong Kong, Kowloon, Hong Kong. E-mail: kinmanyu@cityu.edu.hk
[b] Department of Physics, Comilla University, Kotbari, Cumilla 3506, Bangladesh
[c] Department of Materials Science and Engineering, City University of Hong Kong, Kowloon, Hong Kong
[d] Department of Electrical Engineering and Computer Sciences, University of California, Berkeley, CA 94720, USA
[e] Department of Applied Physics, The Hong Kong Polytechnic University, Kowloon, Hong Kong

† Electronic supplementary information (ESI) available. See DOI: https://doi.org/10.1039/d3tc03166g

phase of $CsPbI_3$ transforms into an orthorhombic yellow phase.[9,20,22,24] The yellow phase may also be termed as the insulating, non-perovskite or δ-phase.[25] This transformation not only changes the crystal structure, but also degrades the optical properties of this ternary $CsPbI_3$ perovskite. The black phase of $CsPbI_3$ exhibits a smaller bandgap (E_g) compared to the yellow phase, and therefore they vary in their application practicality.[9] Controlled substitution of halide anions in ternary $CsPbX_3$ (X = Cl, Br, I), forming quaternary IHP alloys (mixed halide perovskites, *e.g.*, $CsPb(Cl_{1-x}Br_x)_3$), is an effective way to continuously tune the bandgaps of IHPs from ~1.7 ($CsPbI_3$) to 2.9 eV ($CsPbCl_3$).[11,21] Halide anion alloying of the ternary halides not only allows the tuning of the bandgap and thus the emission wavelength, but also enhances the stability of the mixed halides, namely quaternary $CsPb(Cl_{1-x}Br_x)_3$ and $CsPb(Br_{1-x}I_x)_3$ alloys.[11–13,26] However, composition tuning of quaternary IHPs requires precise control of multiple growth parameters and hence can be a challenging task.[27,28] For instance, in solution processing, the growth and composition tuning of IHPs were impeded by the poor solubility of metal halides.[12] Also, in most cases, solution processing produces polycrystalline halide perovskite materials with a high density of defects.[29] On the contrary, chemical vapor deposition (CVD) is a user-friendly materials synthesis technique, which produces high quality nano/microstructured semiconductor materials.[23,28] Also, good control over the growth direction, periodic twinning, crystal structure, *etc.* in CVD synthesis facilitates the growth of high-quality materials with well-defined morphologies.[28,30] Moreover, high temperature and vacuum processed single crystalline materials obtained using the CVD growth technique exhibit improved charge transport properties with reduced trap density.[31]

The intriguing optoelectronic properties of IHPs are strongly influenced by the morphology and dimensionality of the materials.[32,33] Investigation of a variety of structures, including microplatelets,[23] microwires,[34] nanoplatelets,[35] nanorods,[36] nanosheets,[37] nanowires[38] and colloidal nanocrystals,[39] of different IHPs has been reported. Owing to their geometry specified properties and application practicality, these IHP structures have found potential applications in a wide range of devices.[32,40] Among them, IHP microplates, because of their strong influence on local carrier lifetime and electron–hole interactions, are promising for efficient optoelectronic applications,[41,42] and therefore, have attracted considerable research interest recently.

In addition to their distinctive optoelectronic features, the larger light–matter interaction volume along with tunable emission wavelengths made quaternary IHP alloy microplates ideal candidates for nonlinear optical (NLO) applications.[29,43–45] Two photon or multiphoton absorption (TPA/MPA) is a non-linear optical phenomenon that involves the simultaneous absorption of two or a greater number of NIR photons with sub-bandgap energy followed by the subsequent non-radiative and radiative recombination and therefore the emission of a photon in the visible range. Since the process involves below bandgap excitation, photons penetrate deeper into the sample and the excitation occurs more in the bulk, which increases the gain length.[44] Moreover, the deeper photon penetration results in reduced surface photo-absorption and scattering losses[46] and thus less photodegradation.[44] Therefore, materials having TPA/MPA properties have great potential for applications in light modulation,[46] THz generation and detection,[47] optical data storage,[43] multiphoton microscopy,[45] biomedical imaging and photodynamic therapy.[48] Nonlinear optical (NLO) properties, like TPA and MPA, have been widely reported for organic and polymeric materials, while they have been less explored for IHPs.[43] However, compared to well-explored organic NLO materials, a 5–7-fold higher MPA magnitude was reported for IHPs.[43,49] So far, there have been several reports on IHP based TPA/MPA materials,[29,43,49–51] including TPA in $CsPbBr_3$ single crystals[29] and MPA in (Cs, MA)$PbBr_3$ microcrystals,[50] $CsPbX_3$ quantum dots[43] and Cs_4PbBr_6 film.[51] Very recently, enhancement of NLO properties has also been reported for halide anion engineered IHPs.[43] However, from fundamental and technological viewpoints, microstructures, especially microplates, because of their well-defined morphology, high surface area to volume ratio, and larger light–matter interaction volume, are promising for TPA/MPA NLO applications.[29,44,45,50] High quality mixed halide quaternary IHP alloy microplates grown by CVD could, therefore, be ideal TPA/MPA materials, which might further enhance their NLO applications. Until now, reports on the TPA and MPA properties of halide perovskite microplates were mostly restricted to ternary (Cs, MA)$PbBr_3$ microplates,[50,52,53] and no study on the TPA and MPA properties of composition tuned quaternary $CsPb(Cl_{1-x}Br_x)_3$ and $CsPb(Br_{1-x}I_x)_3$ alloy microplates was reported.

Here we report the structural and optical properties of high quality single crystalline all-inorganic cesium lead halide perovskite (IHP) ternary ($CsPbX_3$ (X = Cl, Br, I)) and quaternary ($CsPbX_3$ (X = $Cl_{1-x}Br_x$, $Br_{1-x}I_x$)) alloy microplates synthesized by a single-step CVD process. Composition tuned smooth-faceted halide perovskite alloy microplates show intense and narrow optical emissions covering the visible spectral range of 413–715 nm. In addition, non-linear optical (NLO) properties, for example, two-photon absorption (TPA), are also observed in both quaternary $CsPb(Cl_{1-x}Br_x)_3$ and $CsPb(Br_{1-x}I_x)_3$ alloy microplates. Our results demonstrate the viability of the quaternary IHP alloy microplates for use as frequency upconversion photonic materials, thus extending their application prospects to light manipulation and detection.

2 Results and discussion

Previously we reported whispering gallery mode (WGM) lasing and demonstrated the on-chip white light emission of CVD grown ternary $CsPbX_3$ (X = Cl, Br and I) perovskite alloy microplates.[23] Here, in addition to the ternary $CsPbX_3$ microplates, their mixed-anion halide quaternary extensions, $CsPb(Cl_{1-x}Br_x)_3$ and $CsPb(Br_{1-x}I_x)_3$, are also synthesized by the single step CVD route. A detailed discussion on the CVD growth can be found in the ESI† or elsewhere in the literature.[4,20,23,28,34,35,54] The properties and prospects of the quaternary halide perovskite alloy microplates are presented in the following subsections.

2.1 Structural and elemental analyses

The morphologies of the ternary $CsPbX_3$ (X = Cl, Br, I) and quaternary $CsPbX_3$ (X = $Cl_{1-x}Br_x$, $Br_{1-x}I_x$) alloy microplates were initially investigated by optical and scanning electron microscopy (SEM). Well-defined square like microplates were grown on both c-Al_2O_3 (sapphire) and SiO_2 coated Si substrates (SiO_2/Si). Sharp-edged square microplates of IHP alloys with smooth surfaces observed by both low- and high-resolution SEM imaging suggest that they have good crystalline quality.[20,27] SEM images of typical $CsPb(Cl_{1-x}Br_x)_3$, $CsPb(Br_{1-x}I_x)_3$ and ternary $CsPbX_3$ (X = Cl, Br, I) microplates are shown in Fig. 1(b), (c), and in Fig. S2 (ESI†), respectively. The lateral size of $CsPb(Cl_{1-x}Br_x)_3$ alloy microplates varies between ~5 and 30 μm, with a majority of these structures being <10 μm in lateral dimensions. In comparison, although $CsPb(Br_{1-x}I_x)_3$ alloy microplates shown in Fig. 1(c) appear to be very similar to $CsPb(Cl_{1-x}Br_x)_3$, they have a more uniform lateral dimension of ~10–20 μm. Despite lateral size variations, the thickness of both types of alloy microplates lies in the range of ~300–500 nm. We note that the lateral dimensions and the vertical height profiles of the alloy microplates can be synergistically controlled by tuning the deposition time, precursor quantity in the source materials, and the carrier gas flow rate. Atomic force microscopy (AFM) images showing the smooth surfaces and well-defined morphologies of typical $CsPb(Br_{1-x}I_x)_3$ and $CsPb(Cl_{1-x}Br_x)_3$ alloy microplates are shown in Fig. 1(d) and Fig. S3 (in the ESI†), respectively. The corresponding thickness profiles are presented respectively in Fig. 1(e) and in Fig. S3(b) (ESI†).

X-ray diffraction (XRD) studies confirm that the $CsPbCl_3$, $CsPbBr_3$ and $CsPbI_3$ microplates have, respectively, tetragonal, monoclinic, and orthorhombic crystalline structures. The same crystal structures of pure ternary halides have been reported in the literature.[20] It is known that at high temperature (*e.g.*, ≥47 °C for $CsPbCl_3$; ≥130 °C for $CsPbBr_3$; and ≥305 °C for $CsPbI_3$) the stable phase of all IHPs is cubic. Since all CVD growth processes were carried out at a high temperature of >450 °C, the IHP microplates were first grown in the cubic phase and when they were cooled down to room temperature, they underwent phase transitions to their respective stable room temperature phases.[20,27] XRD patterns of the ternary and quaternary alloy microplate structures are shown in Fig. 1(f). Notice that the (100) diffraction peaks from the quaternary alloys are shifted to diffraction angles between their respective ternary IHPs, indicating the formation of random alloys.

From Fig. 1(f), the lattice parameter of quaternary alloy microplates can be obtained from the shift of the (100) diffraction peak. Hence, the alloy composition '*x*' in $CsPb(Cl_{1-x}Br_x)_3$ and $CsPb(Br_{1-x}I_x)_3$ microplates can be calculated based on the XRD patterns, assuming the virtual crystal approximation (Vegard's law) for their lattice parameters. Elemental composition of the quaternary IHP alloy microplates was also studied by energy dispersive X-ray spectroscopy (EDS) in combination with SEM for both $CsPb(Cl_{1-x}Br_x)_3$ and $CsPb(Br_{1-x}I_x)_3$ alloys. EDS data obtained for various square microplates of a particular sample and for different positions on each square microplate show consistent results, confirming the compositional uniformity of the quaternary halide alloy microplates. EDS analysis and the elemental maps of the representative quaternary $CsPb(Cl_{1-x}Br_x)_3$ and $CsPb(Br_{1-x}I_x)_3$ IHP alloy microplates are shown in Fig. 2. The atomic ratios of constituting elements in the respective alloys are given in the corresponding EDS spectra shown in Fig. 2(a) and (b). EDS results show that the atomic ratios of the two alloys are

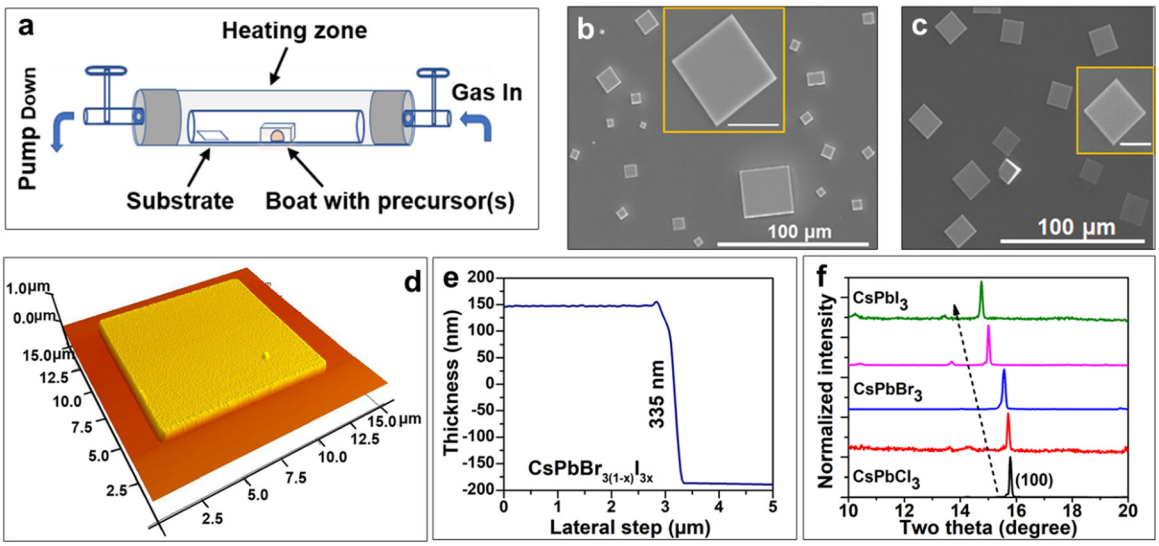

Fig. 1 Growth and microstructures of quaternary IHP alloys. (a) A schematic diagram showing the CVD growth chamber and the relative positions of the precursor and the substrate. (b) and (c) SEM images of typical $CsPb(Cl_{1-x}Br_x)_3$ and $CsPb(Br_{1-x}I_x)_3$ alloy microplate samples, respectively, showing smooth surfaces and clear-sharp edges of alloy microplates obtained by the single-step CVD growth. Insets of (b) and (c) show the enlarged microplate images with 10 μm scale bars. (d) 3D AFM image showing a smooth surface morphology and the corresponding thickness profile (e) of a representative $CsPb(Br_{1-x}I_x)_3$ alloy microplate. (f) XRD patterns of a series of $CsPb(Cl_{1-x}Br_x)_3$ and $CsPb(Br_{1-x}I_x)_3$ alloy samples showing a continuous peak shift due to composition tuning of halide alloys.

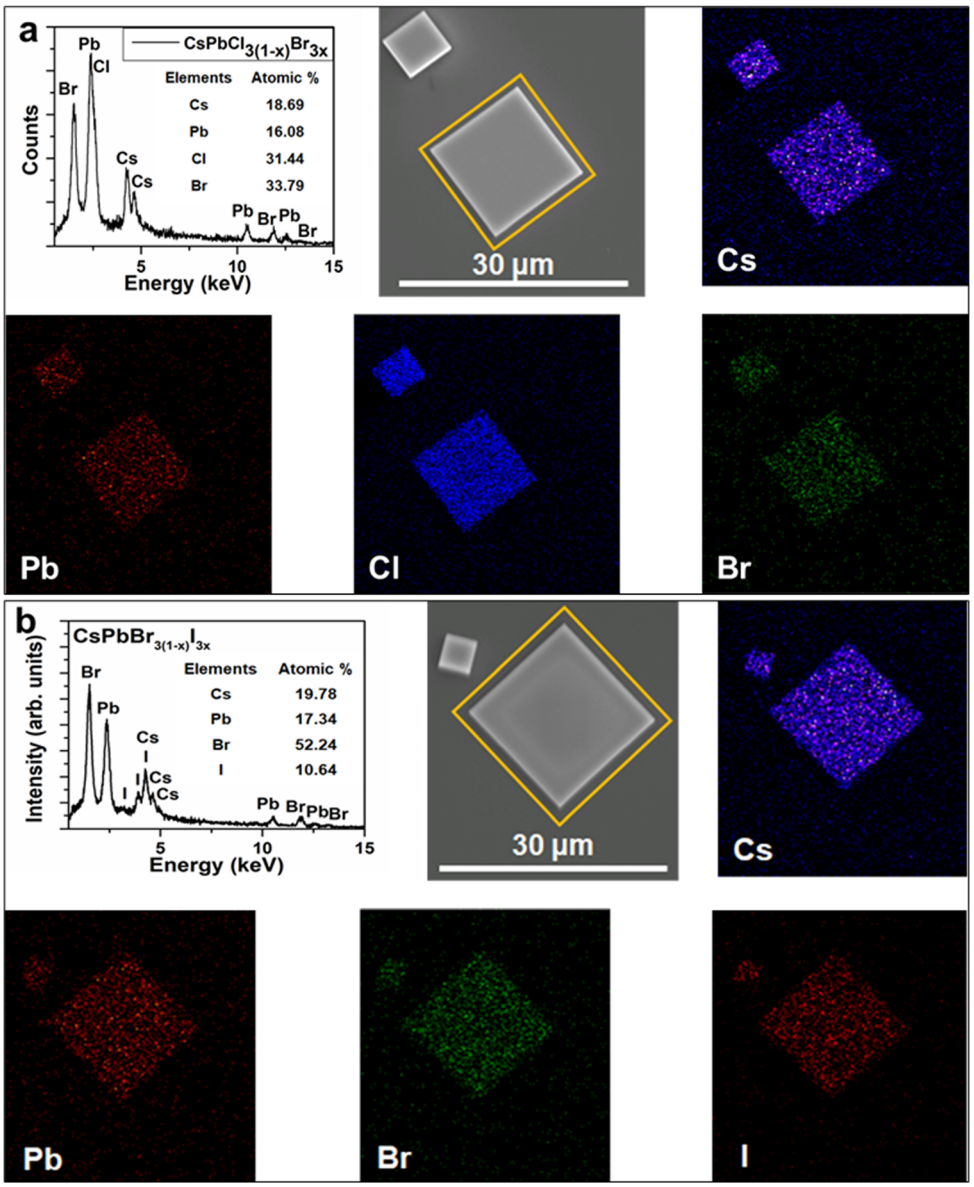

Fig. 2 Alloy compositions of the single-step CVD grown quaternary IHP microplates. The EDS spectra, elemental ratios, SEM images, and corresponding elemental maps of typical (a) $CsPb(Cl_{1-x}Br_x)_3$ and (b) $CsPb(Br_{1-x}I_x)_3$ square microplates, respectively, are presented. Atomic percent contribution of the constituting elements in the respective mixed halide alloys is in good agreement with the halide perovskite general formulation, ABX_3.

Cs : Pb:(Cl : Br) = 18.7 : 16.1: (31.4 : 33.8) and Cs : Pb:(Br : I) = 19.8 : 17.3: (52.2 : 10.6), which are in general agreement with the halide perovskite formulation, ABX_3, and x values of $CsPb(Cl_{1-x}Br_x)_3$ and $CsPb(Br_{1-x}I_x)_3$ are estimated to be 0.60 and 0.17, respectively. The corresponding x values obtained from the XRD calculations are respectively 0.70 and 0.11, which are slightly different from values obtained by EDS analysis. This discrepancy may be attributed to the surface sensitivity of EDS. It should also be noted that x obtained by XRD corresponds to substitutional atoms responsible for changing the lattice parameter, while that by EDS represents atoms present but not necessarily in the lattice. The elemental maps of typical quaternary $CsPb(Cl_{1-x}Br_x)_3$ and $CsPb(Br_{1-x}I_x)_3$ alloy microplates shown in Fig. 2(a) and (b) reveal the even distribution of the constituting elements with no obvious clustering throughout the microplates. In the following, alloy composition x obtained by XRD is used.

2.2 Composition tuning of quaternary IHP alloy microplates

Since the ternary $CsPbX_3$ (X = Cl, Br, I) IHPs have bandgap values of 3.0 eV (X = Cl), 2.3 eV (X = Br) and 1.7 eV (X = I), anion substitution of these materials is expected to produce materials with tunable bandgaps and hence tunable emission peaks covering the entire visible spectrum from 1.7 to 3.0 eV (or λ from 715 to 413 nm). Both quaternary $CsPb(Cl_{1-x}Br_x)_3$ and $CsPb(Br_{1-x}I_x)_3$ IHPs with halide anion content, x, ranging from 0 to 1 were grown by the one step CVD process. Steady state PL measurements were performed on the quaternary IHP alloys using a home-built PL system. Fig. 3(a) shows the continuous

shifting of the PL peaks with the change in the alloy composition, x = Br and I, of $CsPb(Cl_{1-x}Br_x)_3$ and $CsPb(Br_{1-x}I_x)_3$ alloys, respectively. Corresponding true color photographs covering violet (~3.0 eV; 413 nm) to green (~2.3 eV; 529 nm) to red (~1.7 eV; 715 nm) emissions are also shown in the inset of Fig. 3(a). The violet, green and red luminescence colors correspond to emissions from the pure ternary halide compounds $CsPbCl_3$, $CsPbBr_3$, and $CsPbI_3$, respectively.[20,23] The emission peak width (FWHM) values of the alloy microplates are in the range from 85–150 meV, comparable to or even better than the values of those obtained for IHP nano-microstructures grown by hot injection colloidal and CVD syntheses in previous reports.[16,20] These relatively narrow peak widths suggest that the alloy microplates have good crystalline quality with low defect density and small composition fluctuation.[20]

In addition to the steady state PL study, spectrophotometric analysis of the IHP alloy microplates was also performed to estimate the bandgaps of different alloy compositions. A comparison of the room temperature absorbance and steady state PL emission peaks of typical $CsPb(Cl_{1-x}Br_x)_3$ alloy microplates with $x = 0.60$ shown in Fig. 3(b) reveals that the absorption edge closely matches with the PL peak. A very similar phenomenon was also observed for a representative $CsPb(Br_{1-x}I_x)_3$ alloy microplate sample (Fig. S5, ESI†). This suggests that the PL emission corresponds to the band to band emission and is a good measure of the bandgap of the mixed halide quaternary alloys. More generally, for resistive materials like ternary and quaternary halide perovskite microstructures, free carrier effects (Burstein–Moss shift) are insignificant, and the optical bandgap is the same as the intrinsic bandgap. Since the PL emission energy agrees with the absorption edge (as shown in Fig. 3(b)), the PL emission energy corresponds to the fundamental bandgap of the alloy microplates. Here, it is necessary to mention that the probe beam size (~2 mm) in the spectrophotometry setup is much larger than the microplate dimension. Since microplates are randomly dispersed on but do not fully cover the substrate surface, a large fraction of the incident beam goes directly through the substrate. Hence, accurate absorption coefficients (α) of the quaternary microplates cannot be obtained.

As mentioned earlier, the composition of the quaternary alloy microplates was determined by EDS and XRD. We relate the bandgap measured by PL spectroscopy and the composition x calculated from the XRD spectra of both the quaternary $CsPb(Cl_{1-x}Br_x)_3$ and $CsPb(Br_{1-x}I_x)_3$ alloys in Fig. 3(c). A monotonous decrease in the bandgap is observed (from ~3.0 eV ($CsPbCl_3$) to ~1.7 eV ($CsPbI_3$)) with the increase in the x of the respective $CsPb(Cl_{1-x}Br_x)_3$ and $CsPb(Br_{1-x}I_x)_3$ alloys. The composition dependency of the bandgap follows a linear virtual crystal

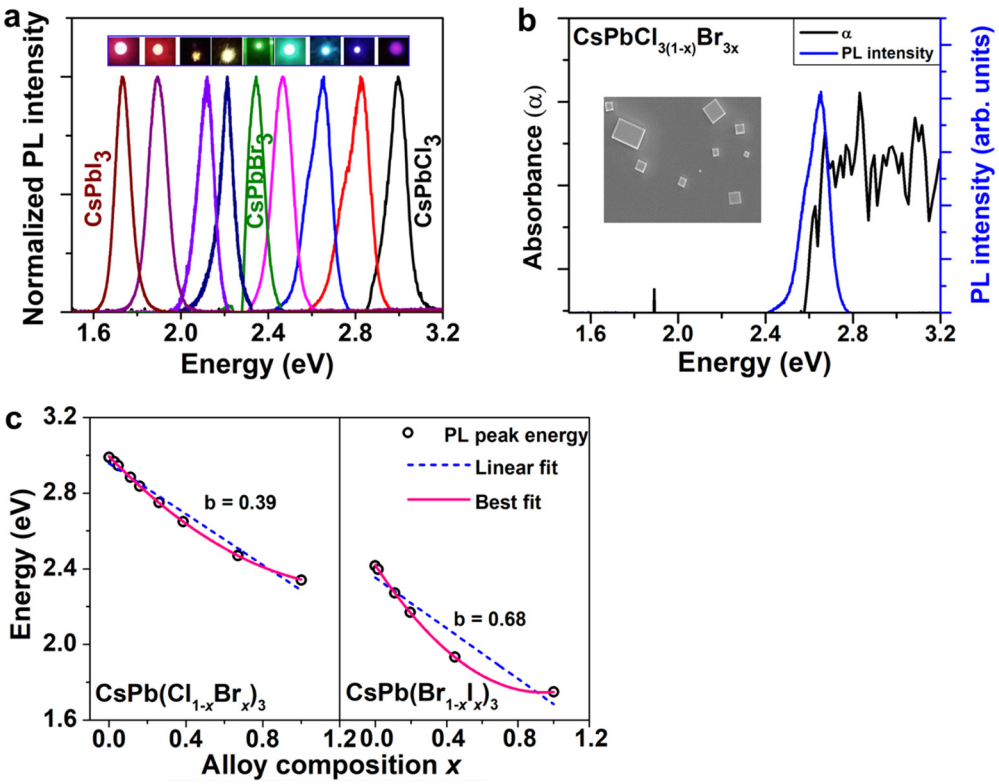

Fig. 3 Optical properties of single-step CVD grown ternary and quaternary IHP alloy microplates. (a) PL emission spectra of pure ternary $CsPbX_3$ (X = Cl, Br, I) and compositionally tuned quaternary $CsPbX_3$ (X = $Cl_{1-x}Br_x$, $Br_{1-x}I_x$) alloy microplates covering the entire visible spectral range. Inset (top) shows true color emissions spots of the respective samples captured during the steady state PL study. (b) Combined absorbance and PL plot of a typical $CsPb(Cl_{1-x}Br_x)_3$ alloy sample with $x = 0.5$. Inset (left) is the scanning electron microcopy image of the corresponding alloy microplate sample. (c) Bandgap changes with the change in the anion halide, x, composition in the quaternary IHP alloy microplates. The pink lines stand for best fits with the bowing parameter b.

approximation (Vegard's law) with small bowing parameters b = 0.39 eV and 0.68 eV for $CsPb(Cl_{1-x}Br_x)_3$ and $CsPb(Br_{1-x}I_x)_3$, respectively.[27] The best fits of the bandgap data using these b values are also shown in Fig. 3(c) as pink solid lines. These bowing parameter values are in good agreement with the previously reported first principles calculated values of 0.48 eV and 0.32 eV obtained for the same materials and the experimentally obtained bowing parameter value of b = 0.33 for $MAPb(I_{1-x}Br_x)_3$.[26,55]

2.3 Composition uniformity and stability of quaternary alloy microplates

A systematic investigation of the lateral and vertical uniformity of the quaternary alloy microplates was performed using a home-built steady state PL setup and a confocal micro-PL mapping facility. Firstly, using a continuous wave (cw) He–Cd laser with λ_{exc} = 320 nm, each sample was illuminated from the front and the back at the same specific location on the sample surface for samples deposited on sapphire substrates as illustrated in the schematic drawing in Fig. 4(a). A similar approach was then adopted and repeated for the full series of $CsPb(Cl_{1-x}Br_x)_3$ and $CsPb(Br_{1-x}I_x)_3$ alloys to obtain the PL emission spectra from various sites on the same sample surface. It is estimated that the penetration depth (90% absorption) of the laser is ~100 nm. The emission peaks from different locations on the same sample are the same with a variation of <10 meV and practically overlap when illuminated from the front and back at the same location, suggesting that the alloy composition is vertically uniform (Fig. 4(b) and (c)). The overlapping of the front and back side PL spectra obtained separately for typical $CsPb(Cl_{1-x}Br_x)_3$ and $CsPb(Br_{1-x}I_x)_3$ alloy compositions is shown in Fig. S4(a) and (b) (ESI†). Secondly, a confocal μ-PL setup, WITec alpha300 R, equipped with an excitation source, λ_{exc} = 532 nm, a charge coupled detector (CCD), and a scanning stage was used to scan the lateral uniformity of typical $CsPb(Br_{1-x}I_x)_3$ microplates. However, our current setup with λ_{exc} = 532 nm is unable to probe $CsPb(Cl_{1-x}Br_x)_3$ microplates with bandgaps >2.3 eV (λ < 530 nm). Note that mixed halide perovskites, especially the iodine based alloys, are known to be sensitive to photoexcitation and photoinduced phase separation.[56] In order to avoid any photoinduced degradation or phase segregation, μ-PL mapping was performed using a laser beam size of ~0.7 μm with an excitation power of 5.0 μW and a mapping time of 5 min. The relatively uniform PL intensity distribution throughout the $CsPb(Br_{1-x}I_x)_3$ (x ~ 0.17) alloy microplate surface shown in Fig. 4(d) suggests that quaternary IHP alloy microplates with uniform material quality are obtained by the single-step CVD process.[57]

In addition to the wide variety of optoelectronic applications, it has also been reported that IHPs exhibit excellent potential for non-linear optical applications, *e.g.*, lasers,[23] frequency up-conversion lasers,[46] *etc.* However, all these applications require high photostability of the materials because of the strong non-linear light–matter interactions involved.[58]

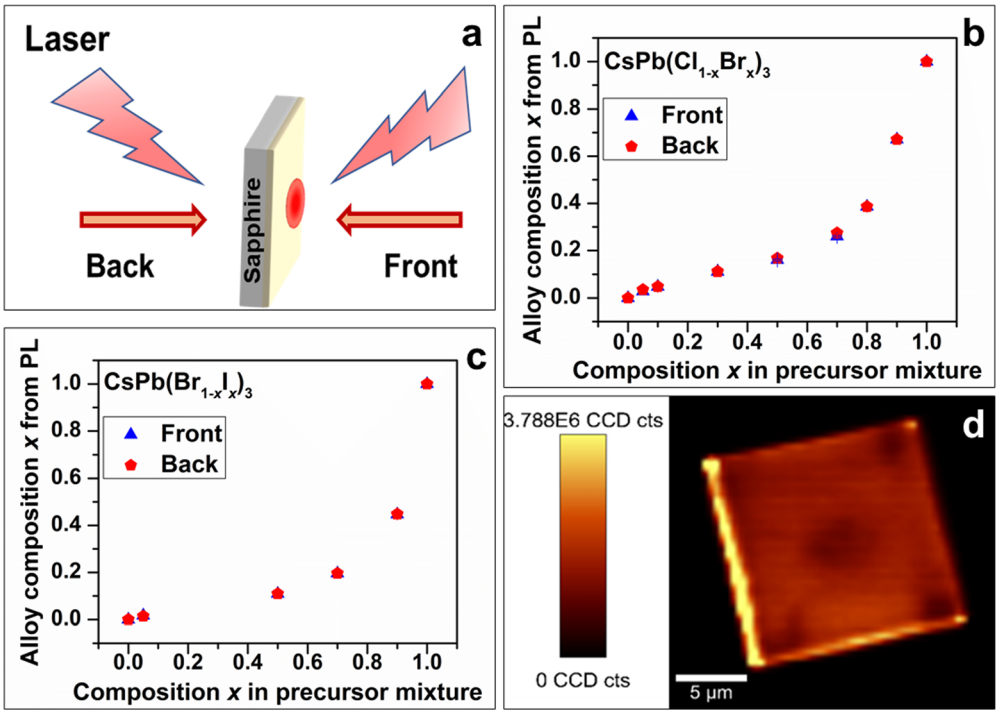

Fig. 4 Composition uniformity of quaternary halide perovskite alloys. (a) A schematic representation of the PL based vertical uniformity study arrangement. Vertical uniformity plots of quaternary (b) $CsPb(Cl_{1-x}Br_x)_3$ and (c) $CsPb(Br_{1-x}I_x)_3$ alloy microplates. Data points denote the alloy composition 'x' obtained with illumination from the front (blue triangles) and back (red pentagons) sides for different alloy compositions in the series. (d) Confocal μ-PL scan of a typical $CsPb(Br_{1-x}I_x)_3$ (x ~ 0.17) alloy microplate. A close to uniform surface intensity distribution shows the lateral uniformity achieved for the single-step CVD grown quaternary IHP alloy microplates.

Although IHPs are considered to be more stable compared to their OHP counterparts,[12] the stability of the quaternary IHP alloys is less well understood. Here, we performed a study of the stability of representative quaternary IHP alloy microplates by PL spectroscopy. PL measurements were performed several times a month on $CsPb(Cl_{1-x}Br_x)_3$ (Fig. 5(a)) and $CsPb(Br_{1-x}I_x)_3$ (Fig. 5(d)) microplates within time periods of 14 and 7 months, respectively. No significant change in both the PL peak positions and peak widths is observed for both alloys. It is important to note that after taking out of the CVD chamber, the samples are stored in a dry box maintained at a relative humidity of ~40%.

The thermal stability of the quaternary microplates was further studied by isothermal and isochronal annealing in air. The isothermal annealing studies were carried out at 100 °C from 0 to 12 hours, while the isochronal annealing studies were performed for 5 min up to 300 °C. Fig. 5(b) and (c), respectively, show PL peak positions and widths of a typical $CsPb(Cl_{1-x}Br_x)_3$ alloy microplate sample after isothermal and isochronal annealing. No significant shift in the PL peak position or broadening of the peak width is observed in Fig. 5(b) and (c), suggesting that the $CsPb(Cl_{1-x}Br_x)_3$ alloy microplates are thermally stable at least up to 300 °C. Similarly, Fig. 5(e) and (f) show that the $CsPb(Br_{1-x}I_x)_3$ alloy sample is thermally stable after both isothermal and isochronal annealing with no shift in the PL peak position. However, the PL peak width of $CsPb(Br_{1-x}I_x)_3$ decreases slightly by ~30 nm after both isothermal and isochronal annealing. This may be due to the removal of defects after post-growth annealing. Note that during all measurements, samples underwent several laser irradiation exposures, at ~100–190 mW cm^{-2} under ≥ AM 1.5 one sun solar irradiation. The insignificant changes observed in the PL peak shift and the PL FWHM values (Fig. 5(e) and (f)) suggest that the quaternary IHP alloy microplates grown by the single-step CVD process also have a high resistance to photodegradation.

2.4 Quaternary $CsPbX_3$ (X = $Cl_{1-x}Br_x$; $Br_{1-x}I_x$) alloy microplates as NLO materials

To understand the NLO properties of quaternary $CsPb(Cl_{1-x}Br_x)_3$ and $CsPb(Br_{1-x}I_x)_3$ alloy microplates, in addition to the normal one-photon absorption (OPA) PL emission, two-photon absorption (TPA) based PL emission properties were investigated. Fig. 6(a) shows a schematic energy band diagram of the two-photon absorption (TPA) and the relevant PL processes. Unlike conventional one-photon absorption, where a single photon with sufficient energy is absorbed, TPA involves the combined energy of two lower-energy photons to achieve the same effect. In the TPA process, two photons with energy lower than the bandgap are absorbed nearly simultaneously ($\Delta t = 10^{-15}$ s), causing an electron to move from the valence band to the conduction band. This process is nonlinear and requires high photon intensity. Subsequent radiative recombination results in the emission of a higher energy photon (corresponding to the bandgap energy) in the visible range as illustrated in Fig. 6(a). The TPA mechanism involved in quaternary $CsPb(Cl_{1-x}Br_x)_3$ and $CsPb(Br_{1-x}I_x)_3$ alloy microplates is initiated by the absorption of an incident photon with E_{photon} = 1.55 eV at (λ_{exc} = 800 nm), which excites a valence band electron to a virtual state, while momentarily ($\Delta t \sim 10^{-15}$ s)

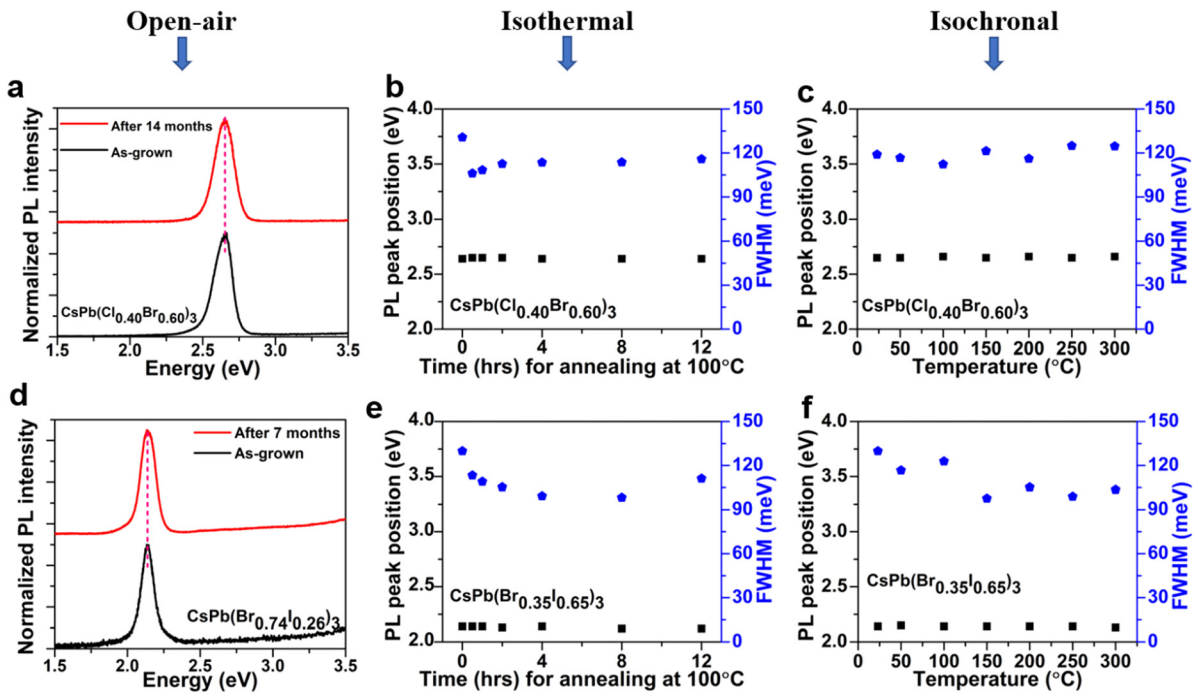

Fig. 5 Stability of quaternary halide perovskite alloy microplates. (a) and (d) Room-temperature ambient-air stability over a period of 14 and 7 months respectively for $CsPb(Cl_{0.4}Br_{0.6})_3$ and $CsPb(Br_{0.74}I_{0.26})_3$ microplates. (b), (c) and (e), (f) Thermal stability of representative $CsPb(Cl_{1-x}Br_x)_3$ and $CsPb(Br_{1-x}I_x)_3$ alloy samples, respectively. PL measurements of microplates after (b) and (e) isothermal annealing at 100 °C for different time periods of 0–12 hours and (c) and (f) isochronal annealing for 300 s in the temperature range between 0 and 300 °C.

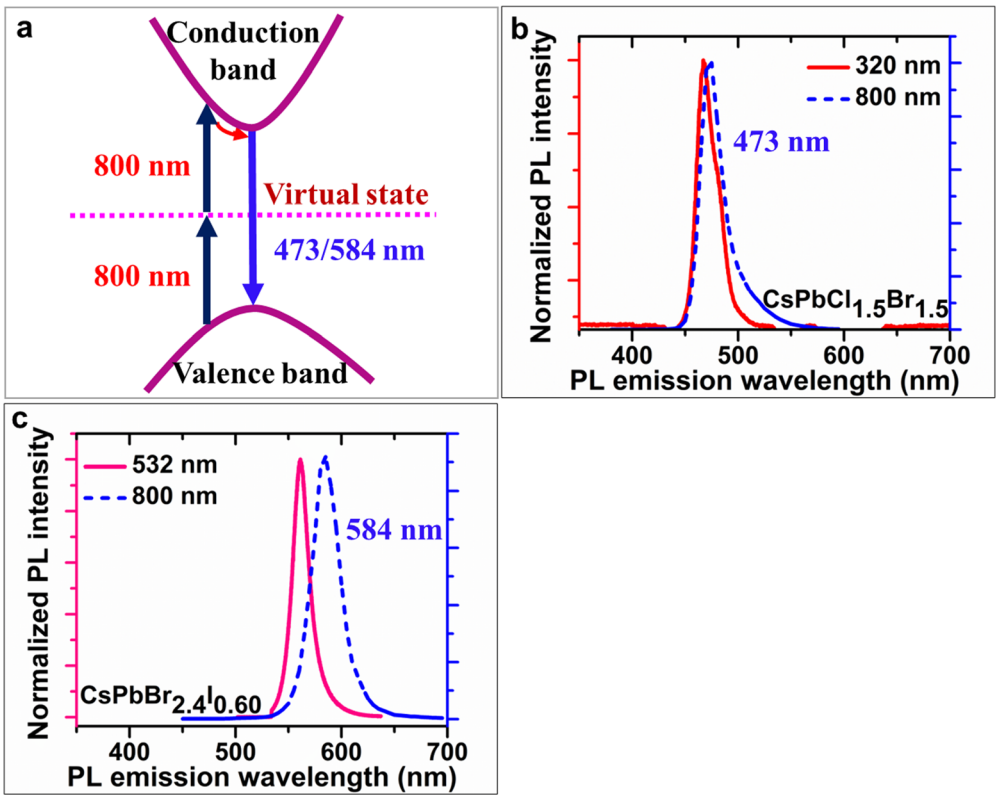

Fig. 6 Two-photon absorption (TPA) in quaternary $CsPb(Cl_{1-x}Br_x)_3$ and $CsPb(Br_{1-x}I_x)_3$ halide perovskite alloy microplates. (a) A schematic illustration of TPA and the corresponding photoluminescence (PL) emission processes. (b) and (c) Normal one-photon (OPA) and two-photon absorption (TPA) PL spectra of $CsPbCl_{1.5}Br_{1.5}$ and $CsPbBr_{2.4}I_{0.6}$ alloy samples. PL spectra in both cases clearly demonstrate the frequency upconversion properties of the quaternary IHP alloy materials.

a second photon with the same energy triggers the virtual state electron to an upper state in the conduction band. The virtual state is a temporary, non-physical intermediate state that exists only for a very short duration, providing a quantum mechanical pathway for the TPA process. It allows the system to absorb the combined energy of two low energy photons and transition to a higher energy state. The excited electron loses its energy through thermalization and hence reaches the conduction band minimum. Finally, the subsequent radiative recombination gives rise to the emission of a visible photon with $\lambda_{emission}$ = 473 nm for $CsPbCl_{1.5}Br_{1.5}$ and $\lambda_{emission}$ = 584 nm for $CsPbBr_{2.4}I_{0.6}$ alloy microplates.

Fig. 6(b) and (c) reveal the TPA related PL spectra of typical $CsPb(Cl_{1-x}Br_x)_3$ and $CsPb(Br_{1-x}I_x)_3$ alloy microplates, respectively. For the $CsPbCl_{1.5}Br_{1.5}$ microplates, normal single photon excitation with λ_{exc} = 320 nm results in a PL emission peak at around 468 nm corresponding to a bandgap of $E_g \sim 2.64$ eV. However, when the microplates were excited with sub-bandgap photons with λ_{exc} = 800 nm (E_{photon} = 1.55 eV), the emission peak is red shifted by 5 nm to 473 nm. Likewise, for $CsPbBr_{2.4}I_{0.6}$ microplates, the PL peak for the TPA process with λ_{exc} = 800 nm is red shifted by ~20 nm relative to the OPA PL obtained for λ_{exc} = 532 nm (Fig. 6(c)). The bandgap of the quaternary $CsPbBr_{2.4}I_{0.6}$ alloy microplates estimated from the OPA PL measurements using λ_{exc} = 532nm is ~2.21 eV ($\lambda_{emission}$ = 561 nm). The red shift of TPA PL emission can be attributed to the increased reabsorption effects due to the larger penetration depth in the TP excitation.[29,52,59,60] The comparatively weaker absorption intensity of the NIR photons (λ_{exc} = 800 nm) allows them to penetrate deeper into the material and therefore excite largely from the bulk. In contrast, above band gap UV (λ_{exc} = 320 nm) or visible photons (λ_{exc} = 532 nm) will be strongly absorbed within a shallow region, which usually causes surface confined excitation and emission.[44] The surface confined excitation and the excitation from the bulk may trigger the OPA and TPA related PL peak shift.[17,61] Moreover, maintaining the excitation at λ_{exc} = 800 nm a series of TPA emission spectra were collected for both $CsPbCl_{1.5}Br_{1.5}$ and $CsPbBr_{2.4}I_{0.6}$ by varying the excitation power. The power dependent fluorescence spectra of the two quaternary alloys are shown in Fig. S6(a) and (b) in the ESI.† Note that the fluorescence peak intensities at ~470 nm and ~580 nm respectively for $CsPbCl_{1.5}Br_{1.5}$ and $CsPbBr_{2.4}I_{0.6}$ increase with the excitation power. The relative fluorescence intensities as a function of the excitation power for the two alloys are plotted in Fig. S6(c) and (d) (ESI†), respectively, for the two alloys. The red lines in Fig. S6(c) and (d) (ESI†) show linear fits of the logarithmic plots. The quadratic dependence of the PL intensity on the excitation power clearly confirms that the emission under 800 nm excitation of the quaternary $CsPbCl_{1.5}Br_{1.5}$ and

$CsPbBr_{2.4}I_{0.6}$ all-inorganic halide perovskite alloy microplates is a TPA induced phenomenon.[17,58,59,62] These observations, therefore, demonstrate that both quaternary $CsPb(Cl_{1-x}Br_x)_3$ and $CsPb(Br_{1-x}I_x)_3$ alloy microplates can act as frequency upconversion NLO materials and have high prospects for their integration into optoelectronic applications, especially in light manipulation and detection related photonic devices. We note that for a complete understanding of the NLO properties of these alloy microplates, the TPA cross–section and structure–property relationship should also be extracted and these will be studied in our future work.

3 Conclusion

We report the properties of ternary $CsPbX_3$ (X = Cl, Br, I) and quaternary $CsPbX_3$ (X = $Cl_{1-x}Br_x$, $Br_{1-x}I_x$) all-inorganic halide perovskite (IHP) alloy microplates synthesized by the single-step chemical vapor deposition (CVD) process. In particular, the nonlinear two photon absorption effect of the quaternary microplates is investigated. The CVD growth can be well controlled to allow us to realize high-quality, single-crystalline alloy microplates with tunable compositions and hence tunable emission wavelengths in the spectral range of 413–715 nm (1.7 to 3.0 eV). These quaternary IHP microplates are compositionally uniform both vertically and laterally, exhibiting intense and narrow PL emissions. Moreover, they are thermally stable and highly resistant to photodegradation. Furthermore, two-photon absorption (TPA) properties are demonstrated for mixed halide quaternary $CsPb(Cl_{1-x}Br_x)_3$ and $CsPb(Br_{1-x}I_x)_3$ alloy microplates, which add a new dimension to the functionalities of these all-inorganic halide perovskites (IHPs) as nonlinear optical (NLO) materials. We believe that this work will open up new avenues for the development of microplate compatible integrated optoelectronic and photonic applications and will certainly enhance the fundamental NLO research.

Data availability

Data are available from the corresponding author only upon request.

Conflicts of interest

There are no conflicts to declare.

Acknowledgements

This work was financially supported by CityU SGP (no. 9380076).

References

1 E. Edri, S. Kirmayer, D. Cahen and G. Hodes, *J. Phys. Chem. Lett.*, 2013, **4**, 897–902.
2 P. F. Ndione, Z. Li and K. Zhu, *J. Mater. Chem. C*, 2016, **4**, 7775–7782.
3 W. J. Yin, Y. Yan and S. H. Wei, *J. Phys. Chem. Lett.*, 2014, **5**, 3625–3631.
4 K. Park, J. W. Lee, J. D. Kim, N. S. Han, D. M. Jang, S. Jeong, J. Park and J. K. Song, *J. Phys. Chem. Lett.*, 2016, **7**, 3703–3710.
5 **https://www.nrel.gov/pv/assets/pdfs/best-research-cell-efficiencies.pdf**, visited on 29 August 2023.
6 J. Song, J. Li, X. Li, L. Xu, Y. Dong and H. Zeng, *Adv. Mater.*, 2015, **27**, 7162–7167.
7 Y. Jiang, M. R. Leyden, L. Qiu, S. Wang, L. K. Ono, Z. Wu, E. J. Juarez-Perez and Y. Qi, *Adv. Funct. Mater.*, 2018, **28**, 1703835.
8 Z. Li, M. Yang, J. S. Park, S. H. Wei, J. J. Berry and K. Zhu, *Chem. Mater.*, 2016, **28**, 284–292.
9 X. Li, F. Cao, D. Yu, J. Chen, Z. Sun, Y. Shen, Y. Zhu, L. Wang, Y. Wei, Y. Wu and H. Zeng, *Small*, 2017, **13**, 1603996.
10 E. T. Hoke, D. J. Slotcavage, E. R. Dohner, A. R. Bowring, H. I. Karunadasa and M. D. McGehee, *Chem. Sci.*, 2015, **6**, 613–617.
11 T. Xu, L. Chen, Z. Guo and T. Ma, *Phys. Chem. Chem. Phys.*, 2016, **18**, 27026–27050.
12 J. B. Hoffman, A. L. Schleper and P. V. Kamat, *J. Am. Chem. Soc.*, 2016, **138**, 8603–8611.
13 J. K. Nam, S. U. Chai, W. Cha, Y. J. Choi, W. Kim, M. S. Jung, J. Kwon, D. Kim and J. H. Park, *Nano Lett.*, 2017, **17**, 2028–2033.
14 Q. Ma, S. Huang, S. Chen, M. Zhang, C. F. J. Lau, M. N. Lockrey, H. K. Mulmudi, Y. Shan, J. Yao, J. Zheng, X. Deng, K. Catchpole, M. A. Green and A. W. Y. Ho-Baillie, *J. Phys. Chem. C*, 2017, **121**, 19642–19649.
15 L. Zhang, X. Yang, Q. Jiang, P. Wang, Z. Yin, X. Zhang, H. Tan, Y. M. Yang, M. Wei, B. R. Sutherland, E. H. Sargent and J. You, *Nat. Commun.*, 2017, **8**, 15640.
16 L. Protesescu, S. Yakunin, M. I. Bodnarchuk, F. Krieg, R. Caputo, C. H. Hendon, R. X. Yang, A. Walsh and M. V. Kovalenko, *Nano Lett.*, 2015, **15**, 3692–3696.
17 Y. Wang, X. Li, X. Zhao, L. Xiao, H. Zeng and H. Sun, *Nano Lett.*, 2016, **16**, 448–453.
18 N. Yantara, S. Bhaumik, F. Yan, D. Sabba, H. A. Dewi, N. Mathews, P. P. Boix, H. V. Demir and S. Mhaisalkar, *J. Phys. Chem. Lett.*, 2015, **6**, 4360–4364.
19 Y. Wang, M. Ibrahim Dar, L. K. Ono, T. Zhang, M. Kan, Y. Li, L. Zhang, X. Wang, Y. Yang, X. Gao, Y. Qi, M. Grätzel and Y. Zhao, *Science*, 2019, **365**, 591–595.
20 Y. Wang, X. Guan, D. Li, H. C. Cheng, X. Duan, Z. Lin and X. Duan, *Nano Res.*, 2017, **10**, 1223–1233.
21 A. Zhang, C. Dong and J. Ren, *J. Phys. Chem. C*, 2017, **121**, 13314–13323.
22 S. Dastidar, D. A. Egger, L. Z. Tan, S. B. Cromer, A. D. Dillon, S. Liu, L. Kronik, A. M. Rappe and A. T. Fafarman, *Nano Lett.*, 2016, **16**, 3563–3570.
23 P. Guo, M. K. Hossain, X. Shen, H. Sun, W. Yang, C. Liu, C. Y. Ho, C. K. Kwok, S. W. Tsang, Y. Luo, J. C. Ho and K. M. Yu, *Adv. Opt. Mater.*, 2018, **6**, 1700993.
24 H. Wang, H. Bian, Z. Jin, H. Zhang, L. Liang, J. Wen, Q. Wang, L. Ding and S. F. Liu, *Chem. Mater.*, 2019, **31**, 6231–6238.
25 R. E. Beal, D. J. Slotcavage, T. Leijtens, A. R. Bowring, R. A. Belisle, W. H. Nguyen, G. F. Burkhard, E. T. Hoke and M. D. McGehee, *J. Phys. Chem. Lett.*, 2016, **7**, 746–751.

26 Z. Zhou, Y. Cui, H. X. Deng, L. Huang, Z. Wei and J. Li, *Appl. Phys. Lett.*, 2017, **110**, 113901.
27 M. K. Hossain, P. Guo, W. Qarony, Y. H. Tsang, C. Liu, S. W. Tsang, J. C. Ho and K. M. Yu, *Nano Res.*, 2020, **13**, 2939–2949.
28 H. Zhou, S. Yuan, X. Wang, T. Xu, X. Wang, H. Li, W. Zheng, P. Fan, Y. Li, L. Sun and A. Pan, *ACS Nano*, 2017, **11**, 1189–1195.
29 C. Zhao, W. Tian, J. Liu, Q. Sun, J. Luo, H. Yuan, B. Gai, J. Tang, J. Guo and S. Jin, *J. Phys. Chem. Lett.*, 2019, **10**, 2357–2362.
30 L. Gil-Escrig, C. Momblona, M. G. La-Placa, P. P. Boix, M. Sessolo and H. J. Bolink, *Adv. Energy Mater.*, 2018, **8**, 1703506.
31 W. Tian, H. Zhou and L. Li, *Small*, 2017, **13**, 1702107.
32 K. Wang, G. Xing, Q. Song and S. Xiao, *Adv. Mater.*, 2020, **33**, 2000306.
33 T. Qiu, Y. Hu, F. Xu, Z. Yan, F. Bai, G. Jia and S. Zhang, *Nanoscale*, 2018, **10**, 20963–20989.
34 Y. Li, Z. Shi, L. Lei, Z. Ma, F. Zhang, S. Li, D. Wu, T. Xu, X. Li, C. Shan and G. Du, *ACS Photonics*, 2018, **5**, 2524–2532.
35 Q. Zhang, R. Su, X. Liu, J. Xing, T. C. Sum and Q. Xiong, *Adv. Funct. Mater.*, 2016, **26**, 6238–6245.
36 T. Yang, Y. Zheng, Z. Du, W. Liu, Z. Yang, F. Gao, L. Wang, K. C. Chou, X. Hou and W. Yang, *ACS Nano*, 2018, **12**, 1611–1617.
37 J. Shamsi, Z. Dang, P. Bianchini, C. Canale, F. Di Stasio, R. Brescia, M. Prato and L. Manna, *J. Am. Chem. Soc.*, 2016, **138**, 7240–7243.
38 M. K. Hossain, R. dos Reis, W. Qarony, Y. H. Tsang, J. C. Ho and K. M. Yu, *J. Mater. Chem. C*, 2021, **9**, 3229–3238.
39 S. Yakunin, L. Protesescu, F. Krieg, M. I. Bodnarchuk, G. Nedelcu, M. Humer, G. De Luca, M. Fiebig, W. Heiss and M. V. Kovalenko, *Nat. Commun.*, 2015, **6**, 8056.
40 W. Qarony, M. K. Hossain, M. I. Hossain, L. Zeng, S. Ma, K. M. Yu, A. Salleo, D. Knipp, C. T. Yip and Y. H. Tsang, *Thin Solid Films*, 2021, **737**, 138950.
41 D. W. DeQuilettes, S. M. Vorpahl, S. D. Stranks, H. Nagaoka, G. E. Eperon, M. E. Ziffer, H. J. Snaith and D. S. Ginger, *Science*, 2015, **348**, 683–686.
42 G. Grancini, A. R. Srimath Kandada, J. M. Frost, A. J. Barker, M. De Bastiani, M. Gandini, S. Marras, G. Lanzani, A. Walsh and A. Petrozza, *Nat. Photonics*, 2015, **9**, 695–701.
43 A. Pramanik, K. Gates, Y. Gao, S. Begum and P. Chandra Ray, *J. Phys. Chem. C*, 2019, **123**, 5150–5156.
44 Z. Y. Zhang, H. Y. Wang, Y. X. Zhang, K. J. Li, X. P. Zhan, B. R. Gao, Q. D. Chen and H. B. Sun, *Phys. Chem. Chem. Phys.*, 2017, **19**, 2217–2224.
45 F. O. Saouma, D. Y. Park, S. H. Kim, M. S. Jeong and J. I. Jang, *Chem. Mater.*, 2017, **29**, 6876–6882.
46 C. Huang, K. Wang, Z. Yang, L. Jiang, R. Liu, R. Su, Z. K. Zhou and X. Wang, *J. Phys. Chem. C*, 2017, **121**, 10071–10077.
47 M. Savoini, L. Huber, H. Cuppen, E. Abreu, M. Kubli, M. J. Neugebauer, Y. Duan, P. Beaud, J. Xu, T. Rasing and S. L. Johnson, *ACS Photonics*, 2018, **5**, 671–677.
48 A. Vangara, A. Pramanik, Y. Gao, K. Gates, S. Begum and P. C. Ray, *ACS Appl. Bio Mater.*, 2018, **1**, 298–309.
49 T. He, J. Li, X. Qiu, S. Xiao, C. Yin and X. Lin, *Adv. Opt. Mater.*, 2018, **6**, 1800843.
50 H. He, E. Ma, X. Chen, D. Yang, B. Chen and G. Qian, *Small Methods*, 2019, **3**, 1900396.
51 K. N. Krishnakanth, S. Seth, A. Samanta and S. Venugopal Rao, *Nanoscale*, 2019, **11**, 945–954.
52 Y. Gao, S. Wang, C. Huang, N. Yi, K. Wang, S. Xiao and Q. Song, *Sci. Rep.*, 2017, **7**, 45391.
53 G. Walters, B. R. Sutherland, S. Hoogland, D. Shi, R. Comin, D. P. Sellan, O. M. Bakr and E. H. Sargent, *ACS Nano*, 2015, **9**, 9340–9346.
54 X. Mo, X. Li, G. Dai, P. He, J. Sun, H. Huang and J. Yang, *Nanoscale*, 2019, **11**, 21386–21393.
55 Y. Zhou, Z. Zhou, M. Chen, Y. Zong, J. Huang, S. Pang and N. P. Padture, *J. Mater. Chem. A*, 2016, **4**, 17623–17635.
56 H. Zhang, X. Fu, Y. Tang, H. Wang, C. Zhang, W. W. Yu, Y. Zhang, M. Xiao and X. Wang, *Nat. Commun.*, 2019, **10**, 1088.
57 X. H. Wang, J. Q. Ning, C. C. Zheng, B. R. Zhu, L. Xie, H. S. Wu and S. J. Xu, *J. Mater. Chem. C*, 2015, **3**, 2589–2592.
58 J. Xu, X. Li, J. Xiong, C. Yuan, S. Semin, T. Rasing and X. H. Bu, *Adv. Mater.*, 2020, **32**, 1806736.
59 Y. Xu, Q. Chen, C. Zhang, R. Wang, H. Wu, X. Zhang, G. Xing, W. W. Yu, X. Wang, Y. Zhang and M. Xiao, *J. Am. Chem. Soc.*, 2016, **138**, 3761–3768.
60 Y. Yamada, T. Yamada, L. Q. Phuong, N. Maruyama, H. Nishimura, A. Wakamiya, Y. Murata and Y. Kanemitsu, *J. Am. Chem. Soc.*, 2015, **137**, 10456–10459.
61 V. D'Innocenzo, A. R. Srimath Kandada, M. De Bastiani, M. Gandini and A. Petrozza, *J. Am. Chem. Soc.*, 2014, **136**, 17730–17733.
62 B. Zhou, M. Jiang, H. Dong, W. Zheng, Y. Huang, J. Han, A. Pan and L. Zhang, *ACS Photonics*, 2019, **6**, 793–801.

